Correlating Lattice Fringe Visibility with Nanocrystal Size and Orientation

W. Qin

*Process and Materials Characterization Lab, MD EL622, APRDL/DDL/Motorola, 2100 E. Elliot Road (85284), Tempe, AZ, USA**

P. Fraundorf and Eric Mandell

Physics & Astronomy, U. Missouri-StL (63121), St. Louis, MO, USA

(Dated: March 31, 2003)

In electron phase contrast imaging of crystals on the nanometer size scale, there arise well-known phenomena which may be attributed to the increased broadening of reciprocal lattice spots as a result of small crystal size: (i) more abundant lattice fringes, (ii) larger uncertainties of fringe spacing when crystal orientations are randomized, and (iii) greater persistence of lattice fringes against variations in crystal orientation. Here we present a method to quantify the probability to visualize cross-fringes along a low-index zone axis. Given the size of the reciprocal lattice spot, lattice fringe visibility after sample orientation change has been successfully predicted for WC_{1-x} nanocrystals, contingent on whether or not the associated reciprocal lattice spots lose intersection with the Ewald sphere.

PACS numbers: 87.64.Bx,87.64.Ee,81.07.-b

I. INTRODUCTION

Nanocrystalline materials have attracted enormous interest primarily due to their high surface to volume ratios, and to new physical and chemical properties that are different from those of the bulk forms[1–5]. Associated with reduction in crystal size is the reciprocal broadening of diffraction intensity, observable in both X-ray diffraction (XRD) and transmission electron microscopy (TEM). In XRD, Scherrer's formula derived more than 100 years ago inversely correlates such broadening with the mass-weighted average grain size[6]. Related phenomena have been observed in high-resolution TEM, where lattice fringes of nanocrystals can be visualized. For example, in simulated high resolution TEM (HRTEM) images of a 1.8 nm spherical Pd crystal, the reciprocal lattice spots were broadened to such a degree that the Ewald sphere intersected spots along more than one zone axis[7]. As a result, fringes appeared destroyed and severely bent along directions that are even $10° - 30°$ away from the [011] axis, and the measured fringe spacings differed from lattice spacings by several, and up to 10 percent. Similarly, estimated fractional uncertainties of the lattice fringe vectors of nanocrystals were reported to become larger for smaller crystals[8]. On the other hand, such reciprocal broadening also increases the abundance of lattice fringes in HRTEM, as well as the persistence of lattice fringes against crystal orientation change. For example, the probabilities of locating 3 linearly independent lattice fringe vectors from a WC_{1-x} crystal for determining the lattice parameters were found to increase with decreasing crystal size[9], and lattice fringes with their normals up to about 20° away from the tilt axis remained visible even after a tilt of about 15°, for crystals whose sizes are between 4 nm and 5 nm[10].

In HRTEM studies of nanocrystals, the following issues are worth addressing: (i) quantitative information about the abundance of lattice fringes, (ii) the ability to distinguish the persistent appearance of an old set of lattice fringes from a new set of fringes, as the crystal orientation is changed, and (iii) quantitative estimation of the uncertainties of fringe spacing from a randomized nanocrystal.

Here we focus on the first two of these. For convenience, our discussion is limited to crystals with a cubic lattice that are randomly oriented and spherical in shape. The radius of a reciprocal lattice spot will be determined by quantifying the probability of cross-fringes along a low-index zone axis. Associated with the intersection of the Ewald sphere with a reciprocal lattice spot, there is one and only one set of lattice fringes in HRTEM image.

For a given crystal structure, there are often only a few generic lattice plane sets that can be resolved within the 1st passband of the contrast transfer function of a given HRTEM. When the sizes of the corresponding reciprocal lattice spots are known, the entire range of crystal orientations relative to the electron beam, within which lattice fringes are visualized, can be determined.

II. METHODS

The first sample used for quantifying the probability to visualize the $\langle 001 \rangle$ zone fringes contains Au/Pd nanocrystals, which were sputtered on a thin carbon film through a Hummer IV Sputter Coater. The second sample used for studying lattice fringe visibility after tilt is a nanocrystalline tungsten carbide thin film, deposited

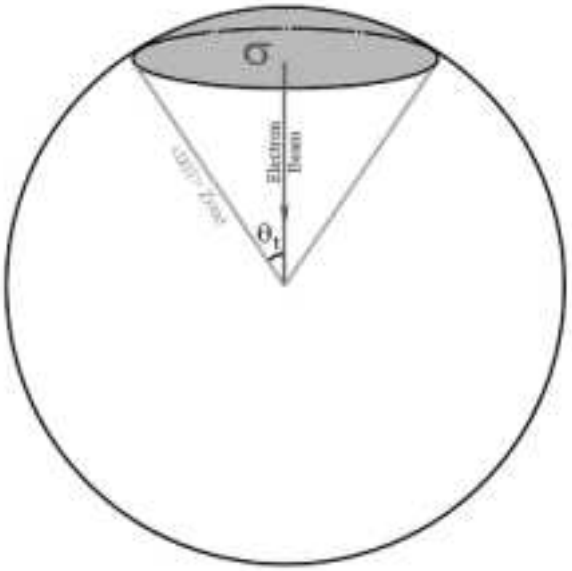

FIG. 1: Schematic illustrating the principle to calculate the probability of seeing cross-fringes along a ⟨001⟩ zone axis of a randomly oriented cubic crystal in HRTEM image. The upper limit for the deviation of crystal orientation from the exact Bragg condition, without losing cross fringes down the zone axis, is expressed as the maximum half-angle θ_t between the zone axis and the electron beam. The solid angle σ thus subtended by a cone with this half-angle θ_t is proportional to the probability that a randomly-oriented crystal will show the cross-fringes along that zone axis.

through PECVD. The TEM used is a Philips EM430ST with a point resolution near 0.2 nm.

III. RESULTS

A. Theory: Cross Lattice Fringe Probability

The radius of a reciprocal lattice spot is expressed as $g_t \equiv f/t$, where f is the visibility factor (to be determined experimentally from the probability that a randomly oriented Au/Pd crystal shows ⟨001⟩ zone cross-fringes in HRTEM images) and t is the crystal diameter.

Figure 1 is a schematic illustrating the principle to calculate the probability, of seeing cross-fringes along a ⟨001⟩ zone axis of a randomly oriented cubic crystal in HRTEM. This probability is denoted as p_x. The maximum deviation of the ⟨001⟩ zone axis from electron beam, without loosing the ⟨001⟩ zone cross-fringes, is expressed as θ_t. The probability p_x strictly proportional to the intersection solid angle σ of orthogonal ⟨001⟩ visiblity bands, and approximately proportional to the solid angle subtended by a circle with half-angle equal to θ_t, i.e.

$$p_{x,\langle 001\rangle}[f,t,d] = 6 \times \frac{\sigma}{4\pi} \approx 3(1-\cos\theta_t[f,t,d]). \qquad (1)$$

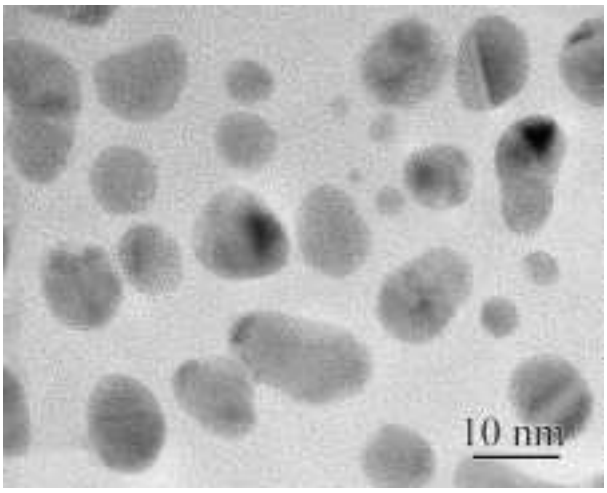

FIG. 2: An HRTEM image of Au/ Pd sputtered on a thin carbon film. Images like this were used to empirically quantify the reciprocal relationship between the diameter (g_t) of the reciprocal lattice spot and that (t) of the crystal, i.e. to determine the visibility factor f in the equation of $g_t = f/t$.

and

$$\theta_t[f,t,d] = \sin^{-1}\left(\frac{g_d^2 - g_t^2 + 2g_t/\lambda}{\sqrt{2}g_d/\lambda}\right), \qquad (2)$$

where λ is the electron wavelength, and $g_d \equiv 1/d$ is the reciprocal lattice spacing. The multiplicity of 6 for ⟨001⟩ zone axes has been taken into account in Equation 1. Derivations of 1 and 2 are given in Appendices A and B, respectively. Here we have limited the crystal to below a certain size, so that even when the electron beam is parallel to the ⟨001⟩ zone axis, the lattice fringes are still visible. This upper limit on crystal thickness is

$$t_o[f,d,\lambda] = \frac{f\lambda d}{\sqrt{d^2+\lambda^2}-d}. \qquad (3)$$

Derivation of equation 3 is given in Appendix C. As will be seen from our experiment, $f \approx 0.79$, so that for Au/Pd particles,

$$t_o[f=0.79, d=2.04\mathring{A}, \lambda=0.0196\mathring{A}] \approx 333.8\mathring{A}, \qquad (4)$$

which is larger than the Au/Pd crystal sizes found in the specimen.

B. Observation: Cross-fringe Probability

In determining f, three HRTEM images of the Au/Pd specimen were analyzed, and a representative image is shown in Figure 2. Please notice that in each "shaded region" there exists more than one single crystal, as is evident from the fact that each set of lattice fringes span an area that is smaller than the whole "shaded region".

TABLE I: Statistics of crystals showing lattice fringes in three HRTEM images of an Au/Pd specimen.

$t[\AA]$	$\langle t\rangle[\AA]$	σ[st]	n	$n_{x,<001>}$	$p_{x,<001>} = \frac{n_{x,<001>}\times 10^{-3}}{3n}$
(20,40)	31.2	5.7	169	5	9.86
(40,60)	50.0	5.9	97	1	3.43

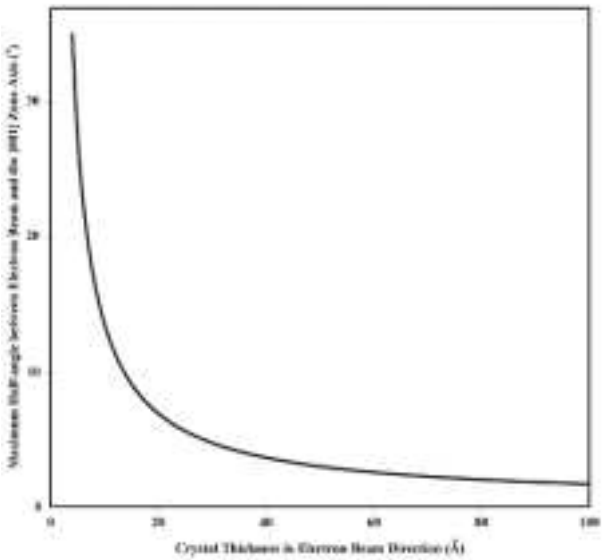

FIG. 3: The maximum angle, θ_t, between a $\langle 001\rangle$ zone of a spherical cubic nanocrystal and the electron beam as a function of crystal diameter. When the $\langle 001\rangle$ zone deviates from the electron beam by an amount that is not greater than θ_t, cross lattice fringes along the $\langle 001\rangle$ zone will remain visible in HRTEM.

As discussed earlier, each Au/Pd crystal in the images is assumed to be randomly oriented and spherical (this is supported by the fact that only about 6.7 percent of the crystals have aspect ratios higher than three, and less than 1 percent above four). Two hundred and sixty-six nanocrystals were identified from the appearance of lattice fringes, and their projection sizes range from 2 nm to 6 nm. Among them 6 show (200) cross fringes along $\langle 001\rangle$ zone axes. The remaining crystals could not be counted individually due to the absence of lattice fringes. Their presence instead was identified through the mass-thickness contrast, i.e., the presence of the "shaded regions" against the bright carbon film background. The total area that these crystals cover is about twice that spanned by those showing lattice fringes. Therefore the total number of nanocrystals is estimated to be three times as the those identified through lattice fringes, i.e., $3 \times 266 = 798$. The statistics are shown in the following Table I.

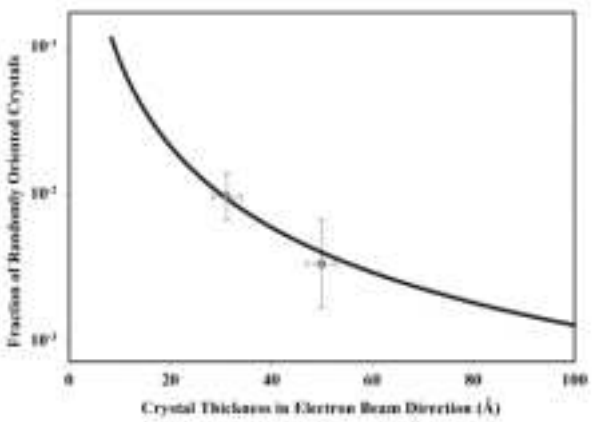

FIG. 4: . Fraction of spherical Au/Pd crystals showing cross lattice-fringes along a $\langle 001\rangle$ zone as a function of crystal diameter, together with the experimental data points obtained from HRTEM images of Au/Pd particles evaporated on a thin carbon film..

C. Determination of the visibility factor

Equation 1 was used to least-square fit the $p_{x,<001>}$ values in Table I, by adjusting f until the relationships

$$p_{x,\langle 001\rangle}[f, t = 31.2\AA, d = 2.04\AA] \approx 9.86 \times 10^{-3}, \quad (5)$$

and

$$p_{x,\langle 001\rangle}[f, t = 50\AA, d = 2.04\AA] \approx 3.43 \times 10^{-3} \quad (6)$$

are true. The value of f thus determined is 0.79. A plot of $\theta_t(f = 0.79, t, d = 2.04\AA)$ is shown in Figure 3. It can be seen that θ_t decreases rapidly over increasing crystal diameter. It drops down to less than ten degrees for $t > 1.4$ nm. For example, θ_t equals 4.75° when t equals 3 nm, and 1.84° when t equals 9 nm. As a result, the solid angles subtended and hence the probabilities of cross-fringes along the [001] zone become very small. For example, the probability p_x is less than 5 percent for $t > 1.4$ nm, as will be seen in the following discussion. A plot of $p_{x,<001>}$ for Au/Pd crystals ($d_{002} = 2.04\AA$) on thin carbon film, as a function of crystal diameter t, together with the two experimental data points, is shown in Figure 4. As shown in the figure, p_x increases greatly as the crystallite size decreases toward a nanometer. However, the "reciprocal broadening", on the other hand, has resulted in an increase in the uncertainties of lattice fringe spacing and interplanar angle as well, for a randomized nanocrystal[11–13].

IV. A WORKING EXAMPLE: PREDICTING LATTICE FRINGE VISIBILITY AFTER TILT

With the availability of the size of the reciprocal lattice spot, predicting lattice fringe visibility against crystal orientation change becomes possible, for WC_{1-x}

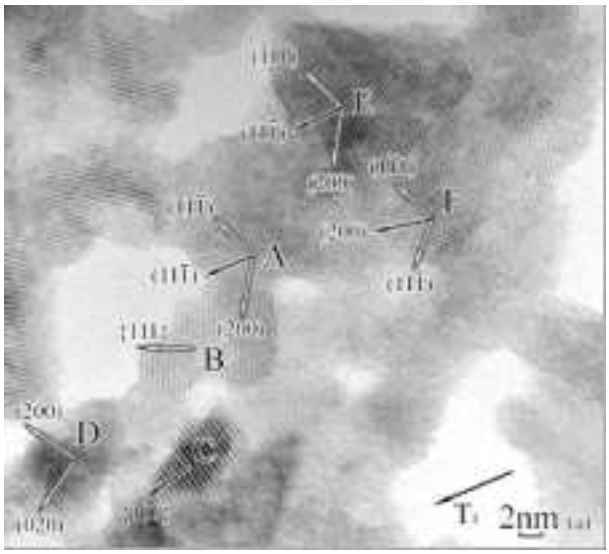

FIG. 5: HRTEM images of six WC_{1-x} nanocrystals showing lattice fringes that become invisible or remain visible after a single tilt of 14.5° around the side-entry goniometer tilt axis. The projection direction of the side-entry goniometer tilt axis T1 is labeled at the bottom right corner of each image. Each lattice plane set has been labeled with both Miller indices and an arrow representing the lattice fringe vector. The length of the arrow is proportional to that of the lattice fringe vector. Here, hollow arrows are used for lattice fringes that are predicted to become necessarily invisible, and solid arrows for those with certain propabilities to do so, in the second specimen orientation shown in Fig 6.

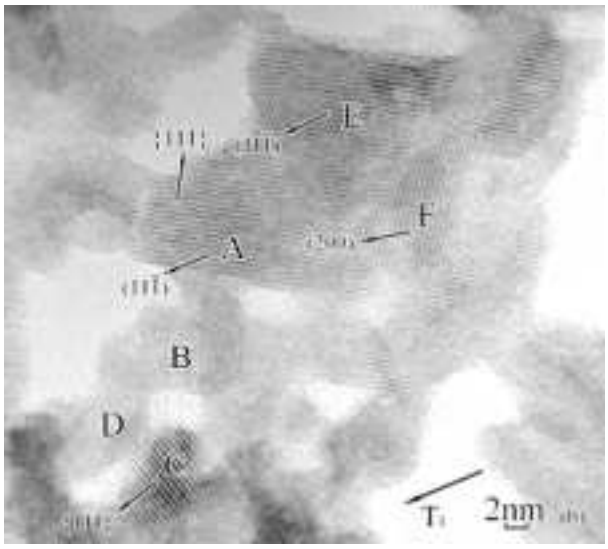

FIG. 6: HRTEM images of the six WC_{1-x} nanocrystals in Fig 5, after a single tilt of 14.5° around the side-entry goniometer tilt axis.

nanocrystals. This is done through determining if the reciprocal lattice spot necessarily loses intersection with the Ewald sphere after tilt, given the angle between the reciprocal lattice vector and the tilt axis, and the amount of tilt used[10]. In order for the reciprocal lattice spot to retain intersection with the Ewald sphere after tilt, the angular deviation of the reciprocal lattice vector from the tilt axis must be under an upper limit which is given as

$$\phi_{max} = \sin^{-1}(\frac{\sin\alpha_{max}}{\sin\frac{\theta}{2}}), \tag{7}$$

where θ is the amount of tilt, and

$$\alpha_{max} = \sin^{-1}(\frac{fd}{t} + \frac{\lambda d}{2}(\frac{1}{d^2} - \frac{f^2}{t^2})) \tag{8}$$

is the maximum angle between the electron beam and the lattice plane, beyond which the lattice fringes become invisible in the image /citeQinThesis. If the reciprocal lattice vector deviates from the tilt axis more than ϕ_{max}, the reciprocal lattice spot will necessarily lose intersection with the Ewald sphere after tilt, and hence the lattice fringes will become invisible after tilt.

Equation 7 and 8 have been used to successfully predict lattice fringe visibility after tilt for WC_{1-x} nancrystals as shown in Figure 5. In the figure, each lattice plane set has been labeled with both the Miller indices and an arrow representing the lattice fringe vector. The length of the arrow is proportional to the magnitude of the lattice fringe vector. Hollow arrows are used for lattice fringes that are predicted to become necessarily invisible, and solid arrows for those with certain propabilities to do so, after tilt, as shown in the Fig 6. Take those three sets of lattice fringes of crystal A shown in Fig 5, which are those of the WC_{1-x} (-1,1,-1), (1,1,-1) and (2,0,0) lattice planes, as examples. The average projection size of crystal A is about $48\mathring{A}$. Equation 7 predicts that for the given amount of tilt

$$\phi(f = 0.79, t = 48\mathring{A}, d_{111} = 2.453\mathring{A}) = 20.6°, \tag{9}$$

and

$$\phi(f = 0.79, t = 48\mathring{A}, d_{002} = 2.124\mathring{A}) = 18.3°, \tag{10}$$

The three lattice fringe vectors deviate from the projection of T_1 by 69.1°, 0.3°, 56.6°, respectively. Among them the first and the third are larger than their corresponding limits obtained in equations 9 and 10. Therefore, the (-1,1,-1) and (2,0,0) lattice fringes are predicted to become invisible after tilt. This is shown to be true in in Figure 6. This way the invisibility of nine out of thirteen lattice fringe sets are predicted, which is consistent with the HRTEM observation. The results are shown in Table II.

In Figure 5, the nine lattice fringe sets which are predicted to become invisible after tilt are labeled with hollow arrows. Please note that all these lattice fringe sets disappear in Fig 6, which is an indication of the consistency of the model with the HRTEM observations.

TABLE II: Correlating equation 7 in predicting lattice fringe invisibility after tilt with HRTEM observation as shown in Figures 5 and 6. Quantities in the third and the fifth columns are obtained from Fig 5 before tilt, and column 7 contains a theoretical prediction of invisibility after tilt for comparison to the experimental result from Fig 6 in column 8.

ID	θ°	$t[\AA]$	(hkl)	ϕ°	ϕ°_{max}	$\frac{\phi}{\phi_{max}} > 1$?	Invisible?
A	14.5	48	(1,1,-1)	0.3	20.6	No	No
A		48	(-1,1,-1)	69.1		Yes	Yes
A		48	(2,0,0)	56.6	18.3	Yes	Yes
B		56	(1,1,1)	24.6	17.8	Yes	Yes
C		42	(1,1,1)	11.8	23.4	No	No
D		46	(2,0,0)	57.5	19.0	Yes	Yes
D		46	(0,2,0)	32.5		Yes	Yes
E		70	(1,1,-1)	2.2	14.5	No	No
E		70	(-1,1,-1)	65.0		Yes	Yes
E		70	(2,0,0)	58.2	13.1	Yes	Yes
F		48	(1,-1,1)	67.1	20.6	Yes	Yes
F		48	(1,1,-1)	43.9		Yes	Yes
F		48	(2,0,0)	11.8	18.3	No	No

As an alternative to the above, Figure 7 shows plots of $\phi_{max}(f = 0.79, t, d_{111} = 2.453\AA)$ and $\phi_{max}(f = 0.79, t, d_{002} = 2.124\AA)$. Also shown in the figure are the experimental data from Figure 5. Hollow symbols are used to label lattice fringe sets that are observed to become invisible after tilt as shown in Figure 6, and solid symbols for the rest. A consistency between the model and experimental observation is indicated, since all the hollow symbols are above their corresponding curves.

With a slight modification of the model, the probability for the lattice fringes to become invisible after tilt may be calculated[11]. The entire spatial region that the lattice planes are visible in HRTEM may also be mapped onto a sphere (or stereo projection)[11,12]. Lastly, based on this quantitative reciprocal relationship between the reciprocal lattice spots and that of the crystal, the probabilities of success in acquiring the three linearly independent lattice fringe vectors from lattice images of randomly oriented grains at two widely varying tilts may be calculated[14].

V. CONCLUDING REMARKS

The range of diffraction intensity distribution in which lattice fringes are visible can be characterized by the size of the reciprocal lattice spot. This ultimately determines the probability of detecting lattice fringes in the HRTEM, as well as the maximum reduction of observed fringe spacings from the lattice spacing. Here we have quantified the reciprocal relationship between the size of the 200 reciprocal lattice spot of a randomly-oriented Au/Pd nanocrystal, and that of the nanocrystal, by matching the $\langle 001 \rangle$ zone axis fringe probabilities predicted by theory with those obtained from experiment. As an example of application, lattice fringe visibility after sample orientation change has been successfully predicted for WC_{1-x} nanocrystals.

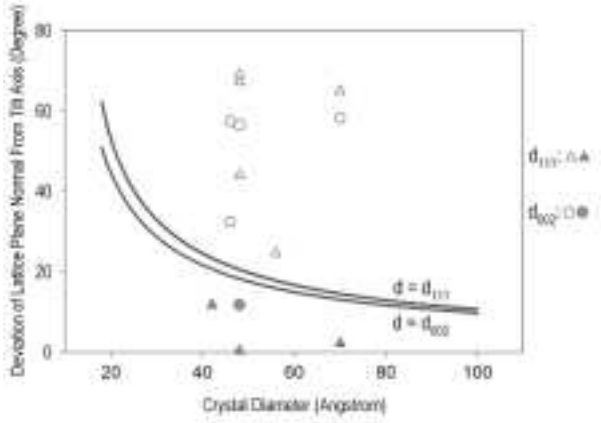

FIG. 7: A plot of the maximum angular deviation of a reciprocal lattice vector from the tilt axis, as given by equation 7, over crystal size. Above such a limit the reciprocal lattice spot necessarily loses intersection with the Ewald sphere after tilting the crystal by 14.5°. Experimental data from Figure 5 and 6 are also shown. The hollow symbols, including both circles and triangles, are used to denote the lattice fringe sets which are observed to become invisible after tilt, and solid symbols for the rest lattice fringe sets. A consistency between the model and the HRTEM observation exists since all the hollow symbols are above their corresponding curves.

APPENDIX A: ESTIMATING BAND INTERSECTION AREAS

A lower limit on the solid angle area of the intersection between great circle visibility bands in Fig. 8 (plus it's analog on the opposite side of the sphere) is given by twice the area of the *inscribed* circle. The area is multiplied by two because great circle bands intersect twice, at opposing points on the orientation unit sphere. An overestimate is twice the solid angle area of the *circumscribed* circle. The band width half-angles may be inferred from lattice spacing, specimen thickness, and electron wavelength from the diffraction geometry described in Appendix B. A simple estimate for the intersection solid angle of bands with half-angles α_1 and α_2, good for small band widths, is twice the area one would calculate for a flat polygon. If the two bands intersect at an angle of ϕ radians, this estimate is $\sigma \approx 2(2\alpha_1)(2\alpha_2)/sin[\phi]$.

Given the value (or an estimate) for this solid angle, the probability of seeing cross fringes in a randomly-oriented particle is then simply $p_x = n\sigma/(4\pi)$, where n is the zone multiplicity (e.g. n=3 for $\langle 100 \rangle$ zone cross-fringes from a cubic crystal).

APPENDIX B: DERIVATION OF VISIBILITY BAND OUTER HALF-ANGLE

Figure 9 illustrates the geometry associated with a simple model of fringe visibility for equant (e.g. spherical)

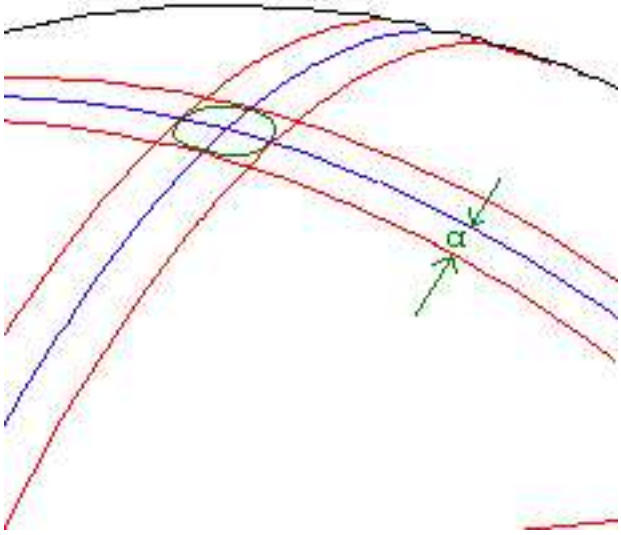

FIG. 8: Visibility bands on the surface of a unit sphere, and a "cross-fringe area" where two bands intersect.

particles. The requirement for visibility is that the reciprocal lattice "spot" intersect the Ewald sphere. The point **O** is the origin of the reciprocal lattice and two reciprocal lattice spots are shown a distance $1/d$ away from the center. Since the effective radius of reciprocal lattice spots is affected by many factors, it is written as $\rho = f/t$, where t is the thickness of the crystal and f is a visibility factor. This visibility factor will be a number on the order of 1 that depends on the method of periodicity detection, the range of angles in the illuminating beam, the microscope's response function, and the amount of "fringe obscuring" noise in the field of the image. It may need to be determined experimentally. As a specimen is tilted, the reciprocal lattice spots will come in and out of contact with the Ewald sphere. In Figure 9, the outermost edge of the reciprocal lattice spot is tangent with the Ewald sphere defining a critical angle, α, at which fringes of the corresponding spacing would be viewable in a direct-space image. We can derive this angle in the following manner.

Since the radius of the Ewald sphere is $1/\lambda$, where λ is the electron wavelength, we can define the length from the center of the Ewald sphere **C** to the center of the reciprocal lattice spot **A** as $1/\lambda - f/t$. The distance from the center of the Ewald sphere to the center of the reciprocal lattice will be $1/\lambda$ and the spacing between the reciprocal lattice spots will be $1/d$. If α is the angle defining the maximum tilt of the reciprocal spot before loss of fringe visibility, then we can use the Law of Cosines for triangle **CAO** to derive

$$sin[\alpha] = \frac{d\lambda}{2}[\frac{1}{d^2} + 2\frac{f}{\lambda t} - \frac{f^2}{t^2}]. \qquad \text{(B1)}$$

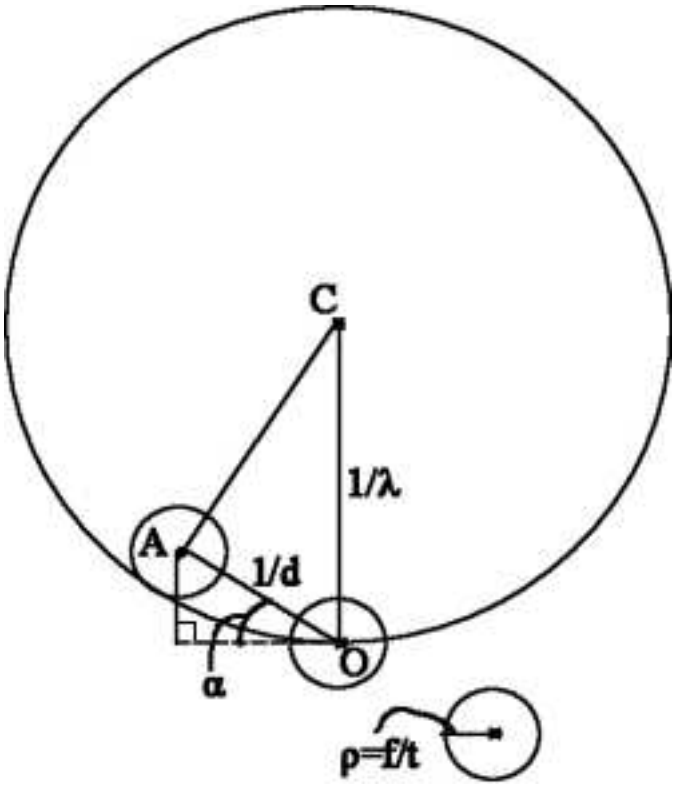

FIG. 9: Ewald sphere geometry for equant-particle fringe visibility. Here **C** is the sphere's center, **O** is the origin of the reciprocal lattice, and **A** is the center of a reciprocal lattice spot.

APPENDIX C: DERIVATION OF INNER HALF-ANGLE CRITICAL THICKNESS

If the specimen is sufficiently thick, or diffracting particle wavelengths are sufficiently large, images taken with a parallel beam might also show loss of fringe visibility when the specimen is oriented on the zone axis, i.e. oriented between Bragg conditions for diffraction from either side of a set of lattice planes. This condition in effect would introduce an "invisibility stripe" down the center of the visibility bands depicted in Fig. 8.

Although the large Bragg angles and thick specimens commonly used in X-ray diffraction would make this a common occurrence there, it is rare in electron microscopy because of the thin nature of the specimens and the small electron wavelength. To confirm this, consider the drawing in Fig. 10.

Following notation in the Appendix B, note that the length of segment **AC** is $1/\lambda + f/t$, the length of segment **BC** is $1/d$, and the length of segment **AC** is $1/\lambda$. Hence from Pythagoras' theorem for the right triangle **ABC** one can solve for t to get

$$t = \frac{fd\lambda}{\sqrt{d^2 + \lambda^2} - d}. \qquad \text{(C1)}$$

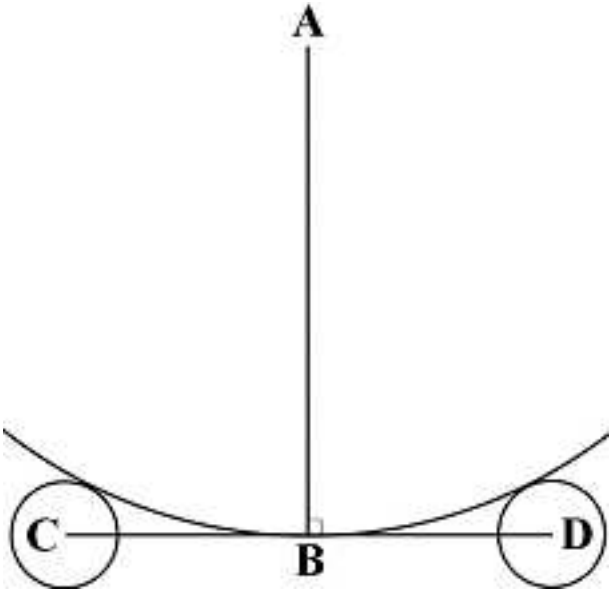

FIG. 10: Schematic configuration with an electron beam traveling down a zone axis, and with reciprocal lattice spots are tangent to the Ewald sphere from the outside. The arc centered at **A** represents part of the Ewald sphere. Segments **BC** and **BD** represent the reciprocal lattice vectors, i.e. $BC = g$ and $BD = -g$. The circles centered at **C** and **D** represent the reciprocal lattice spots. It is obvious **CD** is perpendicular to **AB**.

Putting in typical numbers for these quantities will confirm that this condition is seldom met for specimens thin enough for electron phase contrast imaging, particularly if effects of beam broadening (i.e. a range of angles in the incident beam) are taken into account as well.

ACKNOWLEDGMENTS

This work has benefited indirectly from support by the U.S. Department of Energy and the Missouri Research Board, as well as by Monsanto, and MEMC Electronic Materials Companies.

REFERENCES

* Wentao.Qin@motorola.com

[1] H. Kung and T. Foecke, MRS Bulletin **24**, 14 (1999).
[2] S. Ghosh and O. Inganas, Synthetic Metals **101**, 413 (1999).
[3] D. J. Sellmyer, M. Yu, and R. D. Kirby, Nanostructured Materials **12**, 1021 (1999).
[4] N. Miura, Y. H. Matsuda, K. Uchida, and H. Arimoto, J. Physics - Condensed Matter **11**, 5917 (1999).
[5] B. K. Kim, G. H. Ha, G. G. Lee, and D. W. Lee, Nanostructured Materials **9**, 233 (1997).
[6] B. Cullity (Addison-Wesley Publishing Company, Inc., Reading, Massachusetts Menlo Park, California London Amsterdam Don Mills, Ontario Sydney, 1978).
[7] J.-O. Malm and M. A. O'Keefe, Ultramicroscopy **68**, 13 (1997).
[8] P. Fraundorf, Ultramicroscopy **22**, 225 (1987).
[9] W. Qin and P. Fraundorf, in *Proc. 58th Ann. Meeting* (Microscope Society of America, 2000), pp. 1038–1039.
[10] W. Qin and P. Fraundorf, in *Proc. 58th Ann. Meeting* (Microscope Society of America, 2000), pp. 1040–1041.
[11] W. Qin, Ph.D. thesis, University of Missouri - St. Louis/Rolla (2000).
[12] P. Fraundorf and W. Qin, in *Proc. 59th Ann. Meeting* (Microscope Society of America, 2001), pp. 272–273.
[13] W. Qin and P. Fraundorf, in *Proc. 59th Ann. Meeting* (Microscope Society of America, 2001), pp. 270–271.
[14] W. Qin and P. Fraundorf, Ultramicroscopy **94**(3–4), 245 (2003), cond-mat/0001139.